

Dipoles and streams in two-dimensional turbulence

Javier Jiménez

School of Aeronautics, U. Politécnica Madrid, 28040 Madrid Spain

May 1, 2022

Abstract

Following the suggestion from the Monte-Carlo experiments in Jiménez, J. of Turbul. (2020), that dipoles are as important to the dynamics of decaying two-dimensional turbulence as individual vortex cores, it is found that the kinetic energy of this flow is carried by elongated streams formed by the concatenation of dipoles. Vortices separate into a family of small fast-moving cores, and another family of larger slowly moving ones, which can be described as ‘frozen’ into a slowly evolving ‘crystal’. The kinematics of both families are very different, and only the former is self-similar. The latter is responsible for most of the kinetic energy of the flow, and its vortices form the dipoles and the streams. A mechanism is proposed for the growth of this slow component.

1 Introduction

The subject of this paper originates from the Monte-Carlo simulations in Jiménez (2018, 2020*a,b*), whose purpose was to identify causally significant structures in two-dimensional decaying turbulence by inspecting the effect, after some predetermined time, of randomly perturbed initial conditions. These experiments will not be repeated here, and the reader is directed to the original publications for details. One of the most interesting results was that, besides the expected identification of individual vortices as significant (McWilliams, 1984, 1990*a*), the experiments found that tight dipoles of counterrotating vortices are as causally important as the isolated vortices, or even more so. Modifying a strong vortex in the initial conditions leads to a large perturbation of the flow after five to ten eddy turnovers, but modifying a dipole leads to an even stronger perturbation. Corrotating vortex pairs were not found to be significant in the same way.

The experiments mentioned above were intended to validate the Monte Carlo procedure, as well as to test the fundamental question of whether some localised flow regions are more important than others for the evolution of the flow. They did not pay too much attention to the properties of the flow itself, being restricted, among other things, to a single relatively low Reynolds number. The present paper deals with the fluid mechanics. In particular, it examines whether our understanding of the evolution of two-dimensional turbulence can be improved by the consideration of collective structures, such as the dipoles mentioned above.

Several questions need to be addressed. The first one has to do with the Reynolds number, because one of the results in Jiménez (2020*b*) was that the preferred scale for vortices and

dipoles is about the same, even if the vortices are associated with the enstrophy and the dipoles are structures of the kinetic energy. Spectral analysis shows that the typical scales associated with the two variables are different, but the Reynolds number in Jiménez (2020*b*) was not enough to separate them clearly. To clarify this question, we analyse here flow simulations at several Reynolds numbers, allowing, at least, for some range of scales.

The second question has to do with the role played in the flow by the two ‘templates’ (vortices and dipoles), and perhaps by other structures, because the original analysis was not concerned with the best representation of the flow, nor with flow mechanisms. Its only purpose was to identify the most important structures from the point of view of dynamics, but not the dynamics itself. This problem is also connected with the Reynolds number, because flows at low Reynolds numbers essentially contain a single scale, which represents everything. More general flows are multiscale, and it is usually true that structures that represent well some aspect the flow are not the ones that control the dynamics of others. For example, although vortices and vortex stretching (Vincent & Meneguzzi, 1991) are considered good models for the turbulence energy cascade (Richardson, 1920; Betchov, 1956), it was shown by Jiménez *et al.* (1993) that removing them from the flow had very little lasting effect, and there is clear evidence of intermediate scales of the kinetic-energy that are involved in the cascade process without being directly related to vorticity (Cardesa *et al.*, 2017).

Much of the interest in two-dimensional turbulence originates from the remark by Onsager (1949) that the inviscid evolution of a high-energy system of point vortices results in negative temperature states, and that this would naturally lead to the formation of organised coherent structures, rather than to a disordered flow.

There are at least two ways of approximating high-Reynolds-number two-dimensional turbulence by a conservative Hamiltonian system. The first one is the aforementioned system of point vortices (Batchelor, 1967), and the second is the approximation of the inviscid Euler equations in terms of Fourier components of the velocity truncated to a finite range of wavenumber magnitude (Basdevant & Sadourny, 1975; Lesieur, 2008).

Kraichnan (1967) followed the suggestion of Onsager (1949) to propose that forced two-dimensional turbulence should include a reverse energy cascade towards larger scales, as well as a direct enstrophy cascade towards smaller ones. There is a fair agreement on the mechanism of the enstrophy cascade by means of vortex amalgamation and filamentation (McWilliams, 1990*a*; Carnevale *et al.*, 1991; Benzi *et al.*, 1992). The inverse cascade is less well understood, although it is generally believed that its mechanics is different from that of the enstrophy cascade and, in particular, that it is not predominantly mediated by vortex merging (Paret & Tabeling, 1998; Boffetta *et al.*, 2000; Eyink, 2006; Xiao *et al.*, 2009).

Kraichnan (1967) derived the form of the spectrum of the truncated equilibrium Euler system, and observed that, in the absence of a low-wavenumber dissipation mechanism, energy would tend to accumulate at the largest system scale, in a process similar to the Bose–Einstein condensation of quantum systems. Both the reverse cascade and the condensate (Smith & Yakhot, 1993, 1994) have been numerically and experimentally observed. A fair amount of work has gone into finding equilibrium solutions of the Euler equations that could account for this long-term flow behaviour, from vortex crystals (Aref *et al.*, 2002) to maximum entropy statistics (Joyce & Montgomery, 1973; Montgomery & Joyce, 1974), and there is numerical evidence that forced viscous two-dimensional flow locally relax to these inviscid equilibrium solutions (Montgomery *et al.*, 1992, 1993). For example, numerical forced turbulence in a square box, evolves to a large-scale dipole filling the box diagonally (Smith & Yakhot, 1993). Recent reviews of the

Case	N	L_{init}/L	$q'_0 L/\nu$	$\lambda_{\tau 0}/L$	$\lambda_{\omega 0}/L$	$Re_{\lambda 0}$	$\omega'_0 t_F$	ω'_F/ω'_0	q'_F/q'_0	Symbol
T256	256	0.1	2.3×10^3	0.044	0.184	100	3.3	0.73	0.95	○
T512	512	0.05	4.4×10^3	0.030	0.145	132	18.4	0.69	0.95	△
T768	768	0.025	7.8×10^3	0.025	0.116	197	33.7	0.69	0.96	▽
T1024	1024	0.033	1.1×10^4	0.022	0.105	250	44.9	0.69	0.96	□

Table 1: Parameters of the simulations. The doubly periodic computational box is $L \times L$. The r.m.s. vorticity ω'_0 , and velocity magnitude q'_0 , are measured after the initial discarded transient, decaying from an initial enstrophy spectrum whose peak is at wavelength L_{init} . The Taylor microscale, $\lambda_{\tau 0} = q'_0/\omega'_0$ is used to compute the Reynolds number $Re_{\lambda} = q'_0 \lambda_{\tau 0}/\nu$, and $\lambda_{\omega 0}$ is the enstrophy scale defined in figure 1(a). The number of collocation points used before dealiasing is $N \times N$. The subscript ‘F’ refers to the end of each simulation, so that the decay time after the initial transient is t_F . Case T256 was used in Jiménez (2020b) to identify the causally significant structures used as starting points for the discussion in the text. Each case is an ensemble of 768 independent experiments.

existing work on the reverse energy cascade and on condensate states can be found in Tabeling (2002) and Boffetta & Ecke (2012).

Most of the work on the two-dimensional energy cascade has used forced experiments in which the system eventually settles to a statistically steady state. This has the advantage of allowing the use of ergodicity to compile statistics, but complicates the interpretation of the results, because of the constant interference from the forcing. Decaying turbulence also has an inverse energy flux to large scales (although not necessarily an inverse cascade). The total energy remains approximately constant while its length scale grows until it collides with the domain size. From the point of view of causality characterisation, decaying turbulence has obvious advantages, because things happen only once, and the arrow of time is well defined. On the negative side, compiling reliable statistics requires ensembles of simulations, and analysing the resulting large data sets. In this paper, we study the dynamics of two-dimensional decaying turbulence, with emphasis on the mechanism of the inverse energy flux, using ensembles of simulations at low to moderate Reynolds numbers, guided by the results of the causality analysis mentioned at the beginning of this introduction.

The simulations are described in §2, followed in §3 by the structural analysis of the flow in terms of the vortices, dipoles and streams suggested by the causal analysis. Section 4 describes the collective organisation of the vortices, including their classification into types, and how each type is related to the large scales of the kinetic energy. Section 4.2 proposes mechanisms for this organisation, and §5 concludes.

2 Simulations and basic flow properties

Simulations of decaying nominally isotropic two-dimensional turbulence are performed at various scale disparities in a doubly periodic square box of side L , using a standard spectral Fourier code dealiased by the 2/3 rule. Time advance is third-order Runge-Kutta. The flow field is defined by its velocity $\mathbf{u} = (u, v)$ in the plane $\mathbf{x} = (x, y)$, and by the one-component vorticity $\omega = \nabla \times \mathbf{u}$. It is initialised with random Fourier phases and a fixed isotropic enstrophy spectrum, which is relatively flat for small wavenumber magnitude k , $E_{\omega\omega} \sim k^{3/2}$, and much steeper,

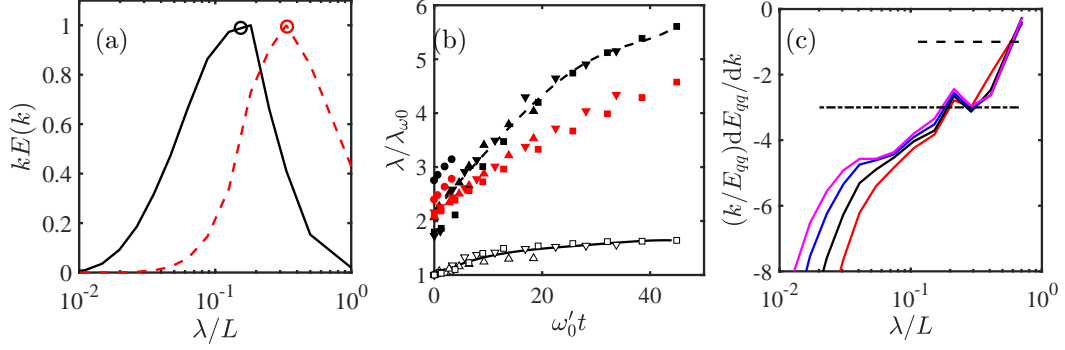


Figure 1: (a) Definition of the enstrophy and energy peak wavelengths. —, Premultiplied enstrophy spectrum; ---, energy spectrum. Case T768 at $\omega'_0 t = 6.3$. (b) Evolution of the enstrophy and energy peak wavelengths; normalized with the enstrophy wavelength at $t = 0$. Symbols as in table 1. Open symbols are enstrophy, and closed black ones are energy. The two polynomial fits are used as reference in later figures. The red closed symbols are the Taylor scale, stretched for clarity to $10\lambda_\tau/\lambda_{\omega 0}$. (c) Logarithmic slope of the energy spectrum at the end of each simulation. From left to right, T1024 to T256. The two horizontal lines mark slopes -1 and -3 , which respectively correspond to the energy and enstrophy peak wavelengths in (a).

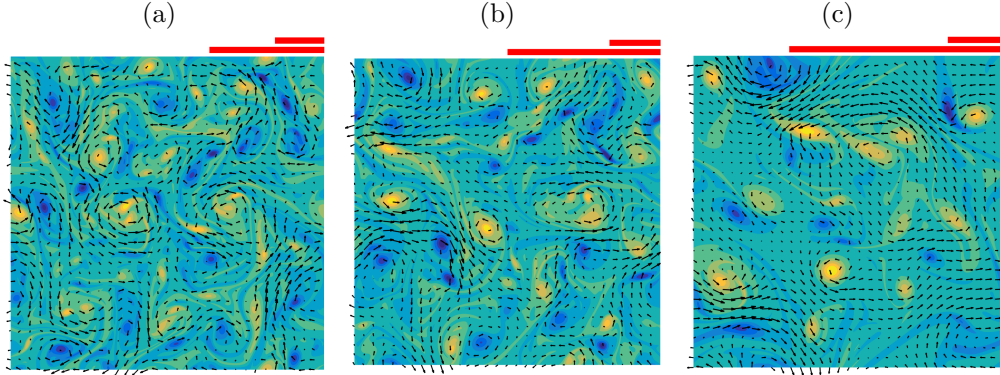


Figure 2: (a) Vorticity and velocity field of a typical flow from T1024. From left to right: $\omega'_0 t = 12.8, 25.6, 64.2$. The shorter bar on top of each figure is λ_ω . The longer one is λ_q .

$E_{\omega\omega} \sim k^{-25/2}$, for large ones. The peak of this initial spectrum, located at $k_{init} \approx 2\pi/L_{init}$, controls the initial energy-containing spectral range. The simulations solve the Navier–Stokes equations in vorticity–stream-function formulation, using regular second-order viscosity, $\nu\nabla^2\omega$.

Natural time and velocity scales can be defined from the root-mean-square (r.m.s.) vorticity magnitude $\omega' = \langle\omega^2\rangle^{1/2}$, where the time-dependent average $\langle\cdot\rangle$ is taken over the full computational box, and $q' = (u'^2 + v'^2)^{1/2}$. The flow is allowed to evolve for $q't_{init}/L = 0.32$ ($\omega't_{init} \approx 6-12$), after which the structures have established themselves. This moment is defined as the start of the simulations, $t = 0$, for the rest of the paper, and is denoted by a ‘0’ subindex in the corresponding quantities. After some experimentation, $\omega'_0 t$ was found to

collapse better the evolution of the different cases, and will be used in the following, although some quantities scale better with $q'_0 t/L$. As the simulation proceeds, the enstrophy decays by approximately 50%, while the kinetic energy decreases at most by 5–10%. A Taylor length scale can be defined as $\lambda_\tau = q'/\omega'$, and used to define a microscale Reynolds number, $Re_\lambda = q' \lambda_\tau / \nu$, where ν is the kinematic viscosity. Both grow by factors of 1.5–2.5 during each simulation, depending on the simulation time. Finally, each experiment is repeated at least 768 times to compile statistics, although a few cases were run twice as many times, to test convergence. These parameters are summarised in table 1.

The evolution of the energy and enstrophy spectra is displayed in figure 1. For each simulation, a time-dependent length scale for the vorticity and for the velocity can respectively be defined by the location of the maximum of the premultiplied enstrophy and energy spectrum, as illustrated in figure 1(a). The enstrophy wavelength $\lambda_\omega = 2\pi/k_\omega$ increases only slowly with time, as shown in figure 1(b), but the energy scale, λ_q , increases as the energy cascades towards larger scales. Eventually, $\lambda_q \approx L$, at which moment the reverse energy flux saturates, and λ_q stops growing (Smith & Yakhot, 1993). Although all our simulations were originally run for $\omega'_0 t \approx 60$, only times for which $\lambda_q/L < 0.6$ are included in figure 1(b) and in table 1. The flow is considered to enter afterwards into a different energy-condensation phase of its evolution, which is not discussed in this paper. Figure 1(c) displays the logarithmic slope of the energy spectrum, and shows that the spectrum develops a short k^{-3} range, corresponding to the classical enstrophy cascade (Kraichnan, 1967; Batchelor, 1969). Note that a slope $(k/E_{qq})dE_{qq}/dk = -3$ corresponds (algebraically) to the maximum of $kE_{\omega\omega} = k^3 E_{qq}$, which defines λ_ω . In the same way, a slope of -1 coincides with λ_q . In the spectra in figure 1(c), all of which are plotted at the end of their simulation, $\lambda_q/L \approx 0.5$.

The Taylor microscale is also included in figure 1(b), on a stretched vertical scale for clarity. It should be noted that, although the Taylor scale is probably little more than an arbitrary length scale in three-dimensional turbulence, it has a deeper significance in two dimensions. We mentioned in the introduction the coexistence of two cascades in two-dimensional turbulence, and that they are connected in a general way with the form of the equilibrium spectrum of the truncated Fourier representation of the Euler equations. The only parameter in this spectrum is the ratio between the total kinetic energy and the enstrophy, which is the squared Taylor scale, and it can be shown that the limiting wavelength between the two cascades is proportional to λ_τ (Basdevant & Sadourny, 1975; Lesieur, 2008). Whether an inverse cascade exists at all depends on whether this limit falls within the truncated set of Fourier wavenumbers, or equivalently, on the ratio λ_τ/L . It is difficult to make this criterion quantitative in viscous flows, whose spectrum is very far from equilibrium, but the growth of this ratio with time in figure 1(b) signals a shift of the kinetic energy towards large scales.

It is interesting that the spectra in figure 1(c) develop a second power-law, k^{-5} , deep within the steep ‘dissipative’ range, especially for the higher Reynolds numbers. Spectra steeper than k^{-3} are well-known in two-dimensional turbulence, and are believed to originate from a variety of reasons that depend on the initial conditions. Saffman (1971) argued that, since vorticity is conserved in the inviscid two-dimensional limit, the mutual distortion of the vortices eventually leads to the formation of vorticity discontinuities whose spectrum is $E_{\omega\omega} \sim k^{-2}$, or $E_{qq} \sim k^{-4}$. Brachet *et al.* (1988), starting from a relatively smooth vorticity field, report that a k^{-4} energy spectrum appears initially, but evolves into k^{-3} after individual vortices appear. This initial time ($\omega'_0 t \approx 10$) is of the same order as the transient period discarded in our simulations.

On the other hand, McWilliams (1984) and Benzi *et al.* (1987), whose initial conditions already include a k^{-3} spectral range, develop a steeper slope in the later part of the decay ($\omega'_0 t \gtrsim 100$ in

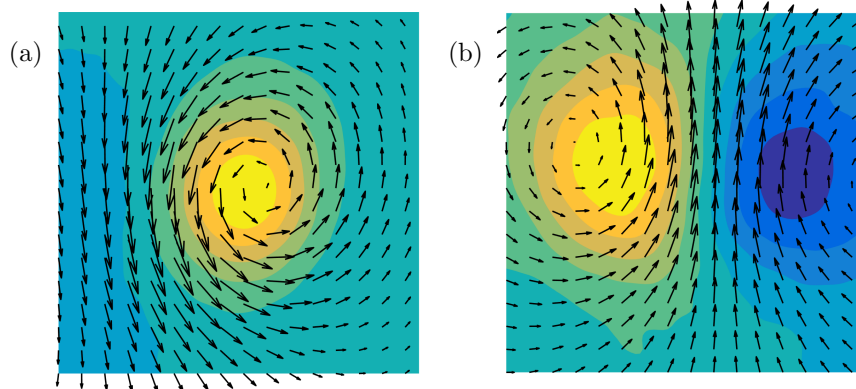


Figure 3: Vorticity and velocity field for the templates identified in Jiménez (2020b) as the most causally relevant flow features. (a) Vortex template, mostly relevant for experiments manipulating vorticity. (b) Dipole template, relevant for velocity manipulations. Because the position, scale and intensity of the templates are adjusted when matching the flow, their orientation, size and intensity are arbitrary.

our notation), when most of the vorticity is organised into individual cores that approximately behave as a conservative Hamiltonian system (Batchelor, 1967). They associate this steeper spectral slope with the vorticity distribution in the cores. This seems to be the case in our simulations, where the k^{-5} plateau only develops towards the energy-condensed end of each simulation. We will mostly be interested in the earlier part of the evolution, where both the vortex cores and the ‘incoherent’ background vorticity are relevant. It should be noted that most of the simulations by the authors mentioned above use high-order hyperviscosity, which favours the formation of isolated vortices, instead of the regular viscosity in this paper. At the moderate Reynolds numbers and regular viscosity of our simulations, the flow is only slightly intermittent. Empirically, the governing parameter for the structure functions of the velocity increments across a distance Δr is the separation compared with the vorticity length scale λ_ω . The fourth-order flatness of the transversal velocity increments reaches $F_4 \approx 4$ for $\Delta r/\lambda_\omega \approx 0.3$, which corresponds to the vortex diameter discussed in the next section. It decays to a slightly sub-gaussian value $F_4 \approx 2.8$ at $\Delta r \approx \lambda_\omega$, and relaxes to the gaussian $F_4 \approx 3$ beyond $\Delta r/\lambda_\omega \approx 2$. The velocity itself is always very close to gaussian.

If we take the wavelengths of the steepest of the two power-law ranges, $\lambda_5 \approx 0.2\lambda_\omega$, to be a measure of the smallest coherent vorticity structures in the flow, the numerical resolution of the simulations in table 1 is $\Delta x/\lambda_5 = 0.1 - 0.2$, in terms of complex Fourier modes, and improves as the simulations proceed.

3 Structural models

As we saw in the introduction, the most interesting structural result in Jiménez (2020b) was that the causally significant flow neighbourhoods in two-dimensional turbulence look either like isolated vortices, or like counterrotating vortex dipoles. The former was expected, because the classical model for this flow is a vortex ‘gas’ (McWilliams, 1984, 1990a; Benzi *et al.*, 1992), but the latter was a mild surprise. The two models were summarised in Jiménez (2020b) by

archetypal ‘templates’, shown in figure 3. After considerable experimentation, the templates were obtained in Jiménez (2020*b*) by conditionally averaging flow patches of a given size, but there is no reason to assume that this is the only scale at which they represent the flow. In fact, Jiménez (2020*b*) showed that an optimal template size from the point of view of flow representation can be determined at moderate Reynolds numbers by a posteriori optimisation of the approximation error between the templates and the test flow fields.

We address in this section whether these results still hold at higher Reynolds numbers, and how the optimum template size changes in those cases.

To test how well a template approximates a particular flow neighbourhood, it is first scaled to size $L_T \times L_T$, optimally oriented (using four orthogonal rotations and one reflection), and its intensity adjusted to match the overall r.m.s. intensity of the flow in question, so that $\langle \xi_T^2 \rangle_T = \xi'^2$, where the ‘T’ subindex represents template properties, as well as averaging over the template domain, and ξ is either the vector velocity or the scalar vorticity. Centring the rescaled template at some point, \mathbf{x} , the representation error is measured as the relative L_2 norm of the difference between the flow and the template,

$$\Phi_\xi(\mathbf{x}, L_T) = \frac{\|\xi(\mathbf{x} + \tilde{\mathbf{x}}) - \xi_T(\tilde{\mathbf{x}})\|_{\tilde{\mathbf{x}} \in T}}{\|\xi\|_T}, \quad (1)$$

which is a function of L_T and of \mathbf{x} . Statistics are compiled over all the positions in an $N_t \times N_t$ ‘test’ grid, and over all the flow realisations, and scanned over L_T .

We address in this section whether these results still hold at higher Reynolds numbers, and how the optimum template size changes in those cases.

To test how well a template approximates a particular flow neighbourhood, it is first scaled to size $L_T \times L_T$, optimally oriented (using four orthogonal rotations and one reflection), and its intensity adjusted to match the overall r.m.s. intensity of the flow in question, so that $\langle \xi_T^2 \rangle_T = \xi'^2$, where the ‘T’ subindex represents template properties, as well as averaging over the template domain, and ξ is either the vector velocity or the scalar vorticity. Centring the rescaled template at some point, \mathbf{x} , the representation error is measured as the relative L_2 norm of the difference between the flow and the template,

$$\Phi_\xi(\mathbf{x}, L_T) = \frac{\|\xi(\mathbf{x} + \tilde{\mathbf{x}}) - \xi_T(\tilde{\mathbf{x}})\|_{\tilde{\mathbf{x}} \in T}}{\|\xi\|_T}, \quad (2)$$

which is a function of L_T and of \mathbf{x} . Statistics are compiled over all the positions in an $N_t \times N_t$ ‘test’ grid, and over all the flow realisations, and scanned over L_T .

Typical probability density functions (p.d.f.s) of the approximation error are given in figure 4(a,b) as functions of the template size. The peak of the histogram generally moves to smaller errors as L_T decreases, and becomes very skewed, especially for dipoles, suggesting the necessity of using several figures of merit to quantify the overall performance of a template. An obvious choice is the mean error, $\langle \Phi_\xi \rangle(L_T)$, where the average is taken over all the template positions. It provides an overall goodness of fit, but the shape of the histograms in figure 4(a,b) suggests that it may mix some very good local fits with some very bad ones. Coherent structures can be important for the flow dynamics even if they fill a relatively small area fraction (Jiménez, 2018), and a representation of the flow in terms of them should be able to stress the good fits even at the expense of de-emphasizing some of the bad ones. A measure with this property is the fraction of the p.d.f. above a given error threshold. We use $P_\xi = \text{prob.}(\Phi_\xi > 1)$. The

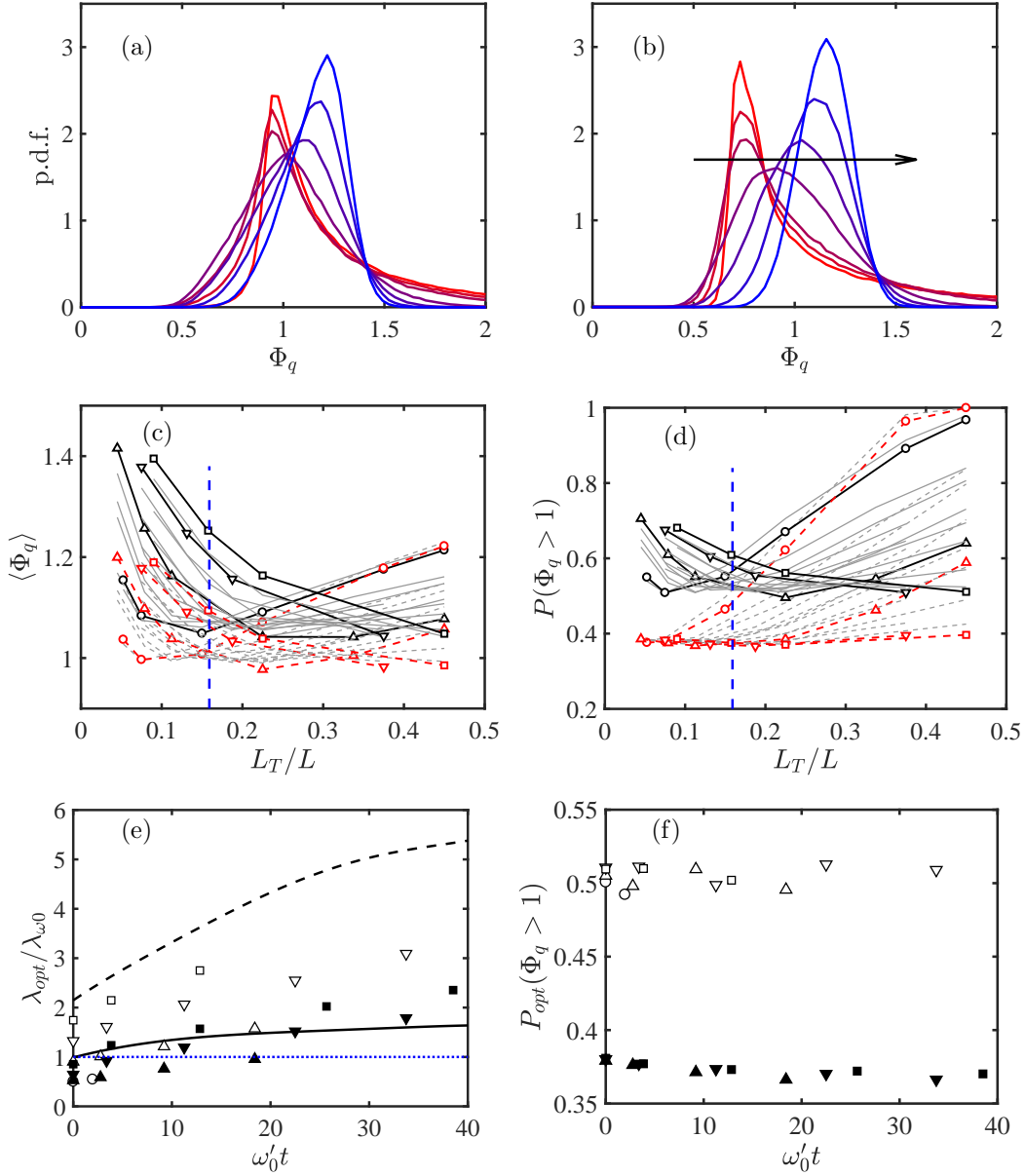


Figure 4: (a,b) P.d.f. of the template approximation error. Energy error norm. Case T512, $\omega'_0 t = 9.2$. Template size, increasing from red to blue: $L_T/L = 0.045, 0.08, 0.11, 0.22, 0.34, 0.45, 0.56$. (a) Template is a vortex. (b) Template is a dipole. The arrow is in the direction of increasing L_T . (c,d) Approximation error as a function of case and of template size. Cases are plotted for different times as grey lines without labels, except for the final time of each simulation, which is highlighted and labelled as in table 1. —, Template is a vortex; ---, template is a dipole. The dashed vertical line is a representative value of λ_ω/L , from table 1. (c) Error is averaged over all template positions. (d) Error measured as the fraction of relative local errors larger than unity. (e) Template size for optimum P_q . Lines are the polynomial fits to λ_ω and λ_q in figure 1(b). Closed symbols are dipole templates; open symbols are vortex templates. (f) As in (e), for the optimum P_q .

behaviour of both measures with template size is shown in figure 4(c,d), and depends on the particular case and on the simulation time considered. Most cases are displayed in the figure as light grey lines, without identification, to show general trends, but the final time of each simulation is highlighted and labelled with the symbols in table 1.

At short simulation times, figure 4(c) shows that the average error, $\langle \Phi_q \rangle$, is minimum for template sizes of the order of λ_ω , but that the optimum size increases with time and with the Reynolds number. The optimum template for some of the longest simulations is the largest one allowed by the computational box, $L_T/L \approx 0.45$. Larger templates are considered in this paper to be contaminated by the box size, and are not included in the analysis. This behaviour holds for vortices (solid lines), and for dipoles (dashed lines).

Figures 4(d) and 4(e) show that the fraction, P_q , of large kinetic-energy error tends to be minimised by small templates of the order of the diameter of the intense vortices seen in figure 2. This fits the intent of this measure, which is to identify local intense structures. It is interesting that this preference for small features is clearest for the dipole template, while the optimum size for the vortex template tends to be larger. Both optimum sizes increase with the evolution time and with the Reynolds number. Figure 4 uses the kinetic-energy norm. The results for the enstrophy norm are similar, with a preference for slightly larger templates.

Figure 4(f) shows that the approximation error attained at the respective optimum sizes changes little among simulations and among simulation times, even if we have seen that the optimum size varies widely. The optimum mean error is approximately $\langle \Phi_q \rangle = 1.04$, $\langle \Phi_\omega \rangle = 1.22$, for vortices and $\langle \Phi_q \rangle = 0.98$, $\langle \Phi_\omega \rangle = 1.12$, for dipoles. The minimum error fraction is $P_q = 0.51$, $P_\omega = 0.81$ for vortices and $P_q = 0.37$, $P_\omega = 0.62$, for dipoles. Interestingly, dipoles are always more successful templates than isolated vortices, and the kinetic-energy error is always lower than the enstrophy one. We will almost exclusively discuss dipole templates and the kinetic-energy norm for the rest of this section.

3.1 Large-scale streams.

Figures 5(a,b) are heat maps for the fit of the vortex and dipole templates to a typical flow snapshot. The intensity in a heat map is proportional to the goodness of fit of the template centred at that point. The darker regions in figure 5 represent better fits, measured by P_q . Figure 5(a) is drawn for vortex templates, and figure 5(b) is drawn for dipoles. In both cases, the size of the template is chosen to be optimum, which in this particular case is different for the two templates. Inspection of the figures shows that the features extracted by the two templates have much in common, although they differ in detail. This is not surprising because a dipole is formed by two vortices, and it was to be expected that at least some of the vortices identified by a vortex template are part of a dipole.

However, the main use of heat maps is not to identify individual features, but to highlight the organisation of the features themselves. Thus, although we have mentioned that figures 5(a) and 5(b) differ in detail, it is visually clear that they cluster around a common large-scale structure, present in both figures. Its nature is clearer in figure 5(c) which shows that it is a meandering stream that spans the full box. This is interesting for two reasons. The first one is that it suggests that the feature detected by the dipole template is not the pair of vortices, but the jet between them. The second one is that those jet segments are part of a larger stream, too large and too irregular to be represented by any local template, but which can be recovered

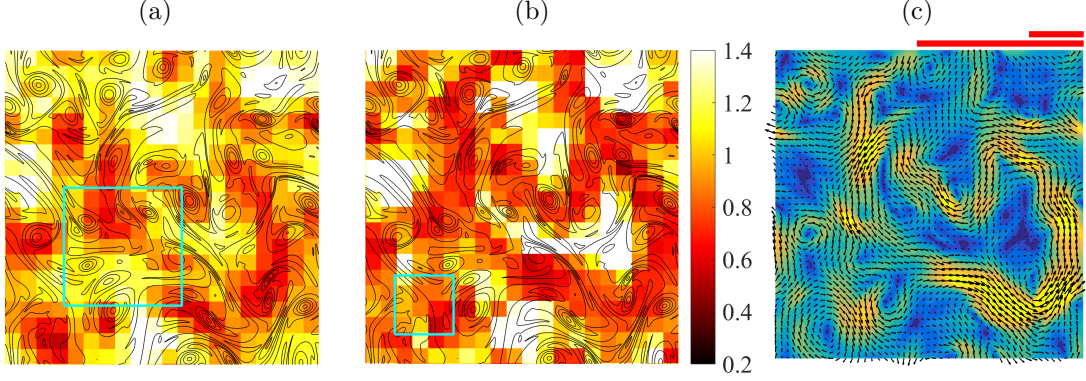


Figure 5: (a,b) Heat maps for the fit error of a typical flow field. Case T768 at $\omega'_0 t = 22$. The cyan box is the size of the template used. Colour represents the approximation error, P_q , for a template centred at each point. Line contours are the vorticity magnitude. (a) Vortex template. (b) Dipole template. (c) Velocity field for the flow in (a,b). The scale bars above the figure are as in figure 2. The background colour is the velocity magnitude, lighter for faster velocities.

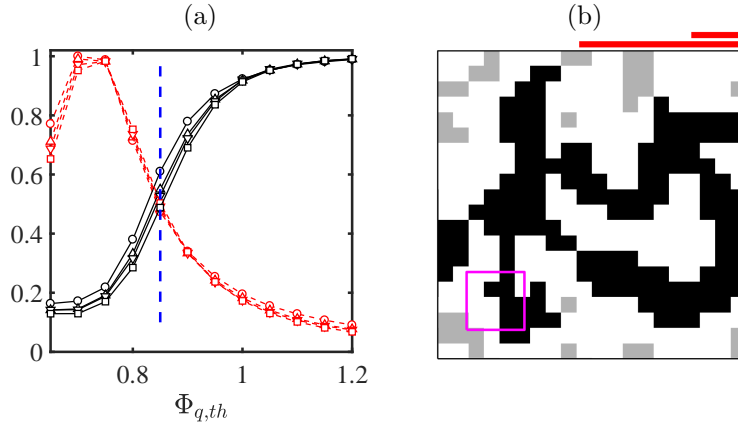


Figure 6: Definition of the largest thresholded structure in each snapshot. (a) Percolation diagram for $\Phi_q \leq \Phi_{q,th}$, as a function of the threshold. Dipole templates optimised for P_q . Solid lines are the area of the largest thresholded object divided by the total thresholded area. Dashed lines are the number of objects. Individual lines are for each simulation, with symbols as in table 1. The vertical dashed line is the standard threshold used below. (b) Thresholded heat map from figure 5(b). The darker object is the largest connected structure, used in the following to represent the large-scale flow organisation.

by the concatenation of several of them.

Figure 6 shows how this large-scale flow organisation can be defined by thresholding the heat map below a given error level. The resulting points are collected into individual objects, defined by contiguity along the four directions of the coordinate axes. Figure 6(a) is the percolation diagram (Moisy & Jiménez, 2004). The solid lines represent the fraction of the total thresholded area contained in the largest contiguous thresholded object. It is unity for very high

thresholds, where a single object fills the whole field, and also for a lowest limit in which a single point represents both the whole thresholded region and its largest object. Neither limit gives information on the structure of the flow, and both are left outside figure 6(a), which centres on the intermediate range in which several individual low-error objects first appear and then merge into larger ones as the threshold is raised. The dashed lines are the number of individual objects, normalised to unit maximum. The percolation diagram is averaged over all the times of each simulation, and varies little among simulations. After some experimentation, the reference threshold is chosen to be $\Phi_{q,th} = 0.85$, which is used in figure 6(b) to threshold the map in figure 5(b). There is a dark largest connected object, and several smaller ones in a lighter colour, which are also below the error threshold but which are not connected to the largest one. They will not be used when compiling the statistics of the large flow scales. The percolation transition is narrow, and changing the threshold by any large amount moves the result into either an empty or a completely full map, but thresholds in the range 0.8–0.9 yield approximately the same results as those presented below.

It should be understood that heat maps and their thresholded versions are at most ‘skeletons’ of flow properties. Each point of the map is an element of the $N_t \times N_t$ ‘test’ grid used to test the template approximation properties. It marks the centre of a template box, but the optimum template size is generally wider than the spacing of the test grid, as shown in figures 5 and 6. Any geometric property of the skeletons should be interpreted with this in mind. For example, the solid lines in figure 7(a) show the inner ‘width’, ρ_1 , of the largest thresholded object in each frame, defined as the side of the largest square that completely fits within the object (Catrakis & Dimotakis, 1996; Moisy & Jiménez, 2004). The figure is compiled over a test grid with $N_t = 20$, so that the minimum possible value is $\rho_1/L = 0.05$. This is smaller than the widths in figure 7(a), which are of the order of $\lambda_{\omega 0} \approx 0.15$ (table 1), but close enough to it to recommend testing whether ρ_1 is influenced by the test grid. Limited testing with $N_t = 30$ prove that the results in figure 7(a,b) could change by approximately by 15–20% on a much finer test grid.

The symbols without lines in figure 7(a) are the integral length,

$$L_{int} = \int_0^\infty C_{\Phi\Phi}(r) dr, \quad (3)$$

derived from the radial autocorrelation function of the approximation error, Φ_q , which typically measures the narrowest dimension of the structures of that variable. It is interesting that, even if we have seen that the approximation error is a marker for the largest, energy-containing scales in the flow, the integral length is narrower than the enstrophy peak in figure 1. In fact, its typical value, $0.3\lambda_{\omega 0} \approx 0.05L$, is of the order of the spacing, L/N_t of the test grid over which it is computed, and could actually be shorter in a finer grid. If we take L_{int} to represent the average thickness of the structures of Φ_q , it would imply that the snapshot in figure 6(b), where the thickness of the structures is of the order of the test cell, is indeed typical.

Note that, since the length of the structures can be estimated by S/ρ_1 , the fact that S and ρ_1 grow at a similar rate in figure 7(a) implies that the length of the structures changes little as the flow evolves ($S/\rho_1 L = 1.3 \rightarrow 1.5$), and that their aspect ratio grows ‘fatter’ ($S/\rho_1^2 = 11 \rightarrow 8$). We will see below that the longitudinal scale of the structures is typically of the order of the box size, and therefore presumably limited by it.

Figure 7(b) shows kinetic energy and enstrophy averaged over dipole templates centred on points within the largest thresholded object in each snapshot. As suggested by figure 5(c), and by the definition of the dipole template in figure 3(b), dipoles contain locally high kinetic energy, but

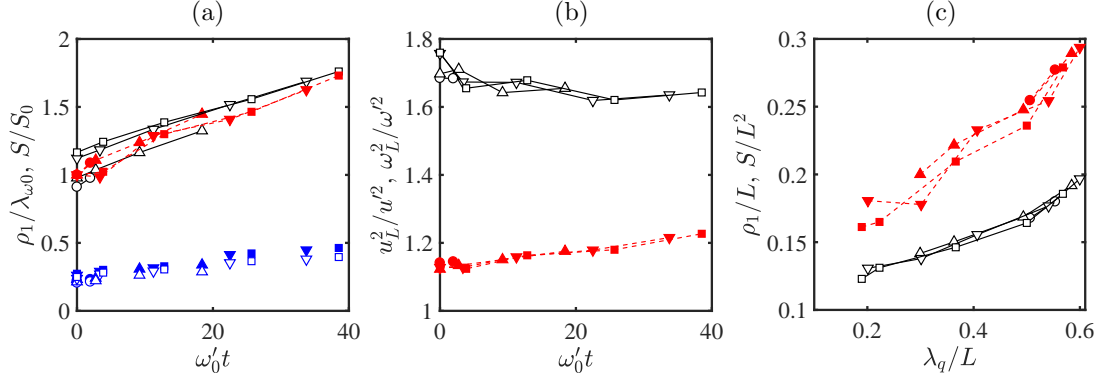


Figure 7: Properties of the largest thresholded structure of low P_q in each snapshot. (a) Temporal evolution of the geometry of the largest structure. —, Inner scale normalised with the initial enstrophy scale, $\rho_1/\lambda_{\omega 0}$; ---, area of the largest structure normalised with its initial value, S/S_0 ; symbols without lines are the integral length $L_{int}/\lambda_{\omega 0}$ for the correlations of Φ_q , defined in eq:Lint. Symbols as in table 1. Open symbols are vortex templates; closed symbols are dipoles. (b) Flow properties within the largest structures. —, kinetic-energy density; ---, enstrophy density. (c) As in (a), but unnormalised, versus the kinetic-energy wavelength.

also moderately high enstrophy. Interestingly, enstrophy is less concentrated than the energy. It could be expected that, since the edge of a jet is necessarily the seat of high vorticity, the ‘fringe’ of grid points surrounding the large-scale thresholded streams would be regions of especially high enstrophy, but this is not true. When energy and enstrophy are conditioned to that fringe, the kinetic energy density is lower than the average, and the enstrophy density is indistinguishable from the mean (not shown). A similar result holds for other flow regions outside the streams. The only high-energy regions are apparently those detected by the dipole template, including the lighter-grey regions in figure 7(b), and the only moderately-high enstrophy regions are also, on average, associated with the streams.

Perhaps the strongest indication of the connection of the streams with the structure of the kinetic-energy is figure 7(c). The quantities in figure 7(a) are normalised with their initial value because they do not otherwise collapse. The initial conditions, which are chosen to provide a variety of scale combinations, are too different to allow it. For example, the average value of the area of the largest stream at $t = 0$ varies by 60% among the different simulations. On the other hand, figure 7(c) shows the unnormalised surface and thickness of the large streams versus the energy wavelength, λ_q . They collapse well, strongly suggesting that the streams are the support of the kinetic energy the flow, and that the process of stream formation is tantamount to the flux of the energy to larger scales.

Figure 8 tests whether the structures detected by the concatenation of dipoles are elongated and aligned with the flow velocity, as suggested by figure 5(c). Consider the sketch in figure 8(a). For a given flow snapshot and template size, each cell in the $N_t \times N_t$ test grid has an associated flow velocity, \mathbf{u} and an approximation error, Φ , defined by averaging over the domain of the optimal template centred on it. Choosing a displacement vector \mathbf{r} with respect to this point, figure 8(b,c) shows the average of the approximation error corresponding to the cell whose centre is closest to the end of \mathbf{r} . The figure shows the mean error conditioned to

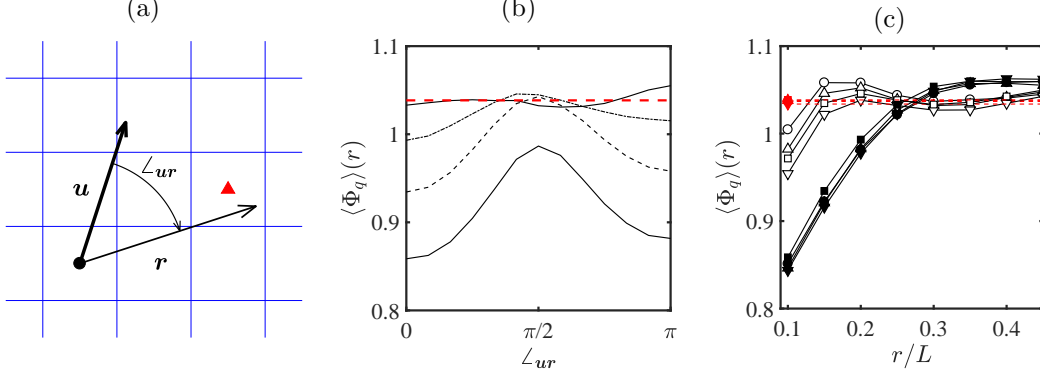


Figure 8: Mean approximation error conditioned to the orientation with respect to the velocity. (a) Definition sketch. (b) Mean error as a function of the orientation angle. T1024 at $\omega'_0 t = 39$. From bottom to top, distance to the reference point: $r/L = 0.1$ (0.05) 0.25. (c) Streamwise and transverse conditional errors as functions of the distance to the reference point. Symbols as in table 1, with each case at its final simulation time. Closed symbols are measured aligned with the velocity, and open ones are measured at right angles to it. The dashed horizontal lines in (b,c) are unconditional errors.

the magnitude of \mathbf{r} and to its angle, $\angle_{\mathbf{ur}}$, with respect to \mathbf{u} . When this conditional mean is averaged over all the points of the test grid, the result is essentially independent of the angle, and similar to the unconditional mean of the error. But, when the conditional centre is chosen within the largest low-error structure in each flow field, figure 8(b) shows that points aligned with the velocity, $\angle_{\mathbf{ur}} = 0$ or $\angle_{\mathbf{ur}} = \pi$, preferentially contain low approximation errors, while those perpendicular to it have high ones. This effect weakens with the length of r , but figure 8(c) shows that it persists for a distance of the order of $0.25L$, which is four or five times longer than the width ρ_1 in figure 7(a). It is interesting that the distance at which the minimum error in figure 8(c) reverts to its unconditional value is approximately the same for the four cases included in the figure. In fact, it changes little among all the cases tested, showing that the longitudinal scale of the high-velocity streams is always of the order of the box size. The growth of the energy wavelength, λ_q , in figure 1(b) and of the area of the high-energy region in figure 7(a) is presumably due to more convoluted streams, rather than to longer-range ones.

An intriguing feature of figure 8(b) is the asymmetry between the conditional error at $\angle_{\mathbf{ur}} = 0$ and $\angle_{\mathbf{ur}} = \pi$. Since each point in the low-error structures is both the origin and the end of some conditioning vector, both directions could be expected to be equivalent. But they are not, and the error is lower in front of the conditioning point than behind it. The effect is small but statistically significant; the estimated standard deviation of the lines in figure 8(b) is only slightly larger than the width of the lines. It is also consistently found in all the cases examined, not only in the one chosen for the figure. This result is difficult to interpret, but the implication is that the velocity is a better predictor of the downstream direction of the low-error structures than of their upstream direction. We will come back to this point in §4.2.

3.2 Vortices

Even if this paper is mostly concerned with the large energy-containing structures of the flow, there is no doubt that two-dimensional turbulence can also be described as a collection of coherent vortices (McWilliams, 1984, 1990*a*; Benzi *et al.*, 1992). The question that interests us here is whether the large-scale structure discussed above for the kinetic energy can be described in terms of the organisation of these vortices. In this section, we first address the properties and evolution of the vortices themselves.

Figure 9(a) shows a segmentation of a typical flow field into individual vortices, defined as connected regions in which $|\omega| \geq H\omega'$. As in the case of figure 7, the vorticity of the flow separates into a few large connected objects for $H \ll 1$, and breaks into more numerous smaller objects as H increases. Beyond a certain threshold, the number of vortices decreases again, and eventually vanishes when no vorticity satisfies the thresholding condition. The value $H = 0.9$ used in figure 9 is chosen to maximise the number of individual vortices (Moisy & Jiménez, 2004). To gain some sense of the importance of vortex interactions, the vortices in figure 9(a) are grouped into co- and counter-rotating pairs. Two vortices are considered a potential pair if their area, s , differs by less than a factor of m^2 , which is an adjustable parameter. The figure uses $m = 2$, but statistics compiled with $m = 1.5$ and $m = 3$ show no substantial differences (see Jiménez, 2020*b*). Vortices are paired to the closest unpaired neighbour within their area class, and no vortex can have more than one partner. Some vortices find no suitable partner, and are left unpaired.

Figure 9(b) displays mean values of the diameter, $s^{1/2}$, and of the distance d between the centres of gravity of the component vortices of the pairs, compiled at several evolution times for each set of simulations. It shows that the diameter of the vortices depends very little on how they are paired. It is approximately 3–4 times smaller than the vorticity wavelength, λ_ω , and of the same order as the k^{-5} plateau in the spectra in figure 1(c). The distance between vortices in the same pair is somewhat larger, closer to the k^{-3} spectral range. The proportionality between the inter-vortex distance and their diameters implies that vortex pairs remain tightly packed at this stage of their evolution, although the average distance grows slightly faster than the diameter, and the area fraction covered by the vortices decays slowly with time (figure 9.c). It should be noted at this point that the intra-pair distance in figure 9(b) offers a possible explanation to the observation in §3.1 that the border of the high-speed streams is not a concentration of high enstrophy. It follows from comparing figures 7(a) and 9(b) that d is two to three times narrower than the width ρ_1 of the dipole-like jets, so that, if these jets are defined as in figure 7, the dipoles are included within the jet, rather than at its border. This is consistent with the visual inspection of the snapshot in figure 5(b).

Figure 9(d) shows the number of vortices involved in different kinds of pairings, giving a rough measure of the importance of the different interactions. Most vortices are in the form of pairs. Of the approximately 2×10^6 vortices represented in figure 9, 43% form dipoles, 29% are in corotating pairs, and 28% are isolated, with a tendency of the number of dipoles and corotating pairs to converge as the Reynolds number increases. Similar values were found by Jiménez (2020*b*) at the lowest of the four Reynolds numbers used in the present paper. The difference between the number of corotating and counterrotating pairs is also present in the covering fraction in figure 9(c), and is a property of the flow that disappears if the vortex position is randomised. The scarcity of unpaired vortices is a geometric property that persists when the pairing algorithm is applied to a set of Poisson-distributed points.

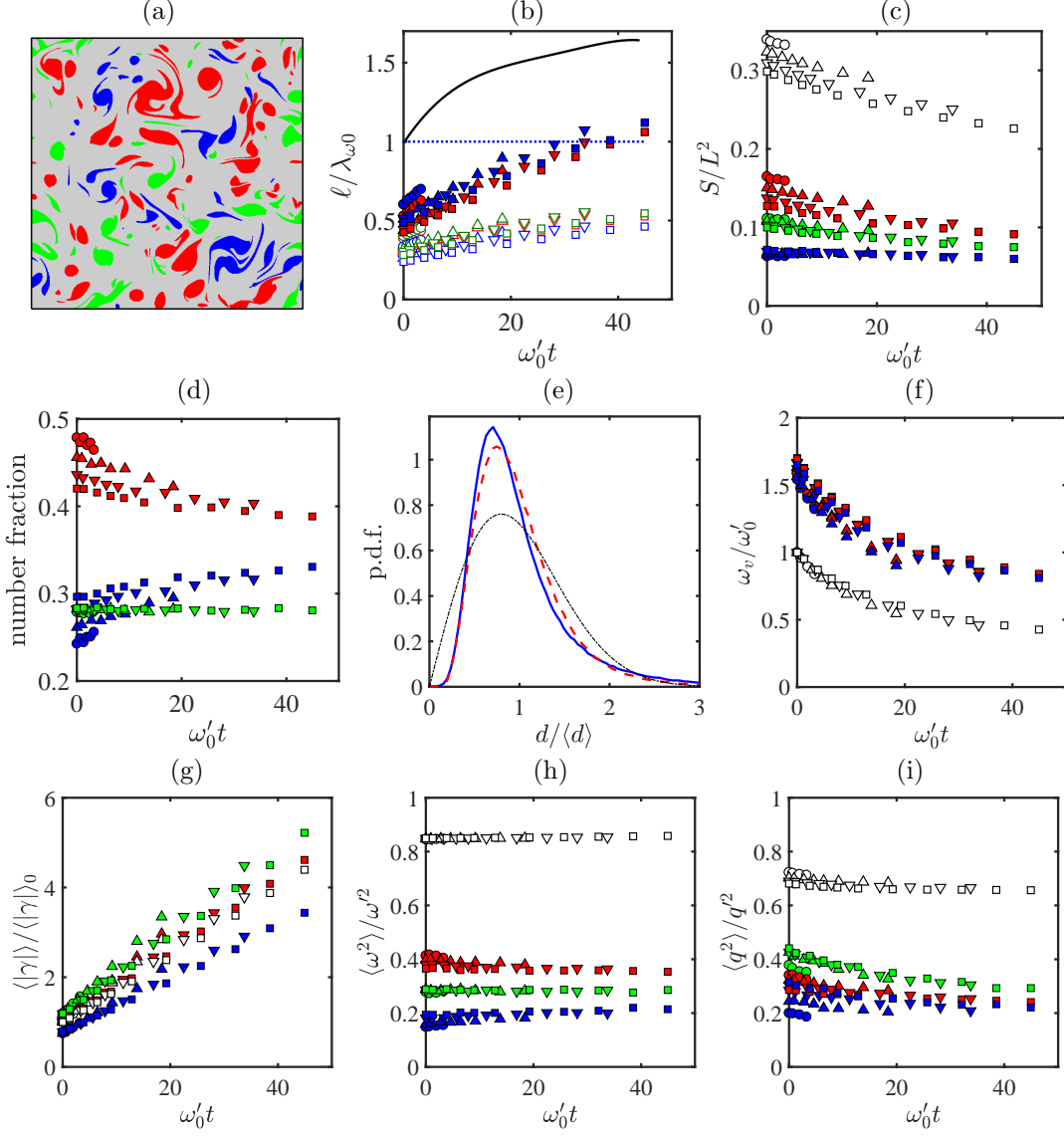


Figure 9: Properties of the thresholded vorticity structures. (a) Typical segmented image. Case T1024, $\omega'_0 t = 39$. In all the panels in this figure, unless otherwise noted, red are dipoles, blue are corrotating pairs, and green are isolated vortices. Other symbols as in table 1. (b) Open symbols are the mean diameter of the vortices, and closed ones are the distance between vortices in a pair. Lengths are normalised with the vorticity wavelength at $t = 0$, and the solid line is the polynomial fit to λ_ω , from figure 1(b). (c) Area fraction covered by all the vortices of a given class. Open symbols include all the classes. (d) Number fraction of vortices in different associations. (e) P.d.f. of the distances between vortices in a pair. Colours as in (a), but the chain-dotted line is the distribution for a Poisson point set. (f) Mean vorticity of the vortex cores. Symbols in (f-i) are as in (c). (g) Average circulation of the vortex cores. (h) Enstrophy fraction contained in the different vortex associations. (i) As in (h), for the kinetic energy.

In fact, a random distribution of the vortex position is a reasonable lowest-order model for their local organisation. Even if the vortex diameter and the intra-pair distance grow by a factor of approximately two during the simulation time, the form of their p.d.f. stays remarkably constant. For example, figure 9(e) shows the p.d.f. of the distance among the components of vortex pairs, normalised by their mean for each individual experiment. The figure also includes the p.d.f of a set of Poisson-distributed points with the same mean. The distribution of dipoles and corrotating pairs are very similar, with a weak tendency of dipoles to be farther apart. The Poisson distribution is wider, but most of the discrepancy can be explained by the exclusion of pairs whose separation is smaller than the vortex diameter (see appendix A). This explanation is confirmed by the distribution of the distance d between all possible couples of vortices (not shown). This distribution should be proportional to d for any homogeneous flow, but this is only true for $d \gtrsim 2\langle s^{1/2} \rangle$. Shorter distances are essentially missing.

In the same way, there is relatively little difference between the properties of vortices in dipoles and those in corrotating pairs. We saw in figure 9(b) that their diameters are similar, and figure 9(f) shows that so are their vorticities, which decay at the same rate as the r.m.s. vorticity of the flow. On the other hand, some explanation is needed for figure 9(c,d), which shows that both the number of dipoles and the total area covered by them is larger than those of corrotating pairs. A similar difference appears in figure 9(g), which shows that the average vortex circulation magnitude grows linearly for all classes. The circulation of a vortex core can only grow by merging with other cores or by entraining background vorticity, since there is no vorticity source in two-dimensions, but the average over a class is also influenced by the transfer among classes. Figure 9(g) shows that the circulation of dipoles is typical of the overall average (they are the largest contributors to it), but that corrotating pairs grow more slowly, while unpaired vortices grow slightly faster than the average. The simplest explanation is that corrotating pairs tend to merge into single (initially unpaired) cores (Meunier *et al.*, 2005), thus depleting their number, while dipoles are longer-lasting (Flierl *et al.*, 1980; McWilliams, 1980).

Figure 9(h) shows the fraction of overall enstrophy contained in the thresholded vortices. Over 85% of the total enstrophy is contained in them, and this fraction is remarkably constant among Reynolds numbers and time, no doubt, in part, because the vorticity threshold used to identify them is a constant fraction of the r.m.s. vorticity. The contribution to the enstrophy of the different vortex classes is in line with the area fraction in figure 9(c), as could be expected from the similarity of vortex properties discussed above.

The fraction of the kinetic energy due to the vortices is harder to define. The simplest definition is the fraction of q'^2 retained by a flow reconstructed from the vorticity contained within a given class of thresholded vortices. Figure 9(i) shows that keeping all the thresholded vortices retains 65–70% of q'^2 . Keeping only the dipoles or the corrotating pairs retains 25–30% of the energy, while keeping only the unpaired vortices retains 30–40%. The change in the relative contribution of dipoles to the enstrophy in figure 9(h) and to the energy in figure 9(i) is interesting. While dipoles predominate in number, area, and enstrophy, their contribution to the energy is of the same order as the corrotating pairs, and substantially less than the unpaired vortices. In fact, even if dipoles contain a local jet of high velocity, their overall kinetic energy is lower than for corrotating pairs, because the total circulation of a dipole is zero, and its induced velocity falls with distance much faster than for a corrotating pair (Batchelor, 1967). Even if decaying turbulence is very far from an equilibrium system, Benzi *et al.* (1992) have shown that an approximately Hamiltonian system of point vortices, punctuated by the occasional merger of like-signed vortices, is a good approximation to the late stages of two-dimensional enstrophy decay. The difference in the interaction energy of dipoles and corrotating pairs is probably also

part of the reason for their different behaviour, and for the slower decay of the former through amalgamation.

In summary, the vortex evolution discussed in this section is consistent with the description of decaying two-dimensional turbulence as a system of discrete vorticity structures (McWilliams, 1984; Benzi *et al.*, 1987; Brachet *et al.*, 1988), although at the relatively early stage of the decay studied here the structures cannot be described as either equilibrium or isolated. Their self-similar growth through amalgamation accounts for the gradual increase in the vorticity scale, λ_ω , but the sizes involved are always much smaller than the energy scale, λ_q (see the scale bars in figure 2).

4 Collective structures

4.1 Vortex organisation

In fact, the question of how vortices organise themselves to create the streams discussed in §3.1 remains open. One possibility, already mentioned, is that the streams are concatenations of dipoles that are responsible for short segments of the stream. We saw in the discussion of figure 9 that this model is compatible with the observed vortex distances and dimensions, but the open question is how the individual dipoles align themselves into longer units. Another model is that the streams are contact interfaces between large-scale vortices. We saw in figure 9(b) that the mean vortex diameter increases only weakly during even the longest flow evolution, and that it is always much smaller than the kinetic-energy wavelength, but it is possible that the small cores organise themselves into large-scale vortex ‘bags’ that fill the space between the streams, acting as coherent structures from the point of view of the kinetic energy (Paret & Tabeling, 1998; Tabeling, 2002). However we saw in §3.1 that the only concentration of vorticity is within the coherent jets, not between them.

The crucial uncertainty is the intensity of the interaction among vortex cores, and whether, for example, the advection velocity of the cores is mainly due to their closest neighbour, or to a background of ‘field’ vortices. The former would support the first of the two models above, while the latter would support the second. Consider vortex pairs. The result of the mutual induction among two vortices of the same sign and similar circulation is a rotation around each other. If the vortices are denoted by A and B , and we estimate the (vector) ‘mobility’ of a vortex by averaging the flow velocity over its core,

$$\mathbf{u}_{vor} = s_{vor}^{-1} \int_{vor} \mathbf{u} \, ds, \quad (4)$$

the induced mobilities in a corrotating pair would be $\mathbf{u}_A = -\mathbf{u}_B$, and the velocity of the centre of the pair would vanish, $\mathbf{u}_{cg} = (\mathbf{u}_A + \mathbf{u}_B)/2 = 0$. On the other hand, dipoles self-induce a common translation velocity, and $\mathbf{u}_A = \mathbf{u}_B = \mathbf{u}_{cg}$. If we define $q_{vor} = \|\mathbf{u}_{vor}\|$, a self-inducing corrotating pair would be characterised by $q_{cg} \ll q_{pair} \equiv (q_A + q_B)/2$, while a dipole would satisfy $q_{cg} \approx q_{pair}$. This is tested in figure 10(a), and it is only satisfied by slow-moving vortices. The behaviour of fast pairs for which $q \gtrsim q'$ is independent of whether they are co- or counter-rotating, and they can therefore be assumed to be mostly advected by a background velocity field.

Figure 10(b) shows that vortex pairs can be classified into two groups. The ‘nose’ extending

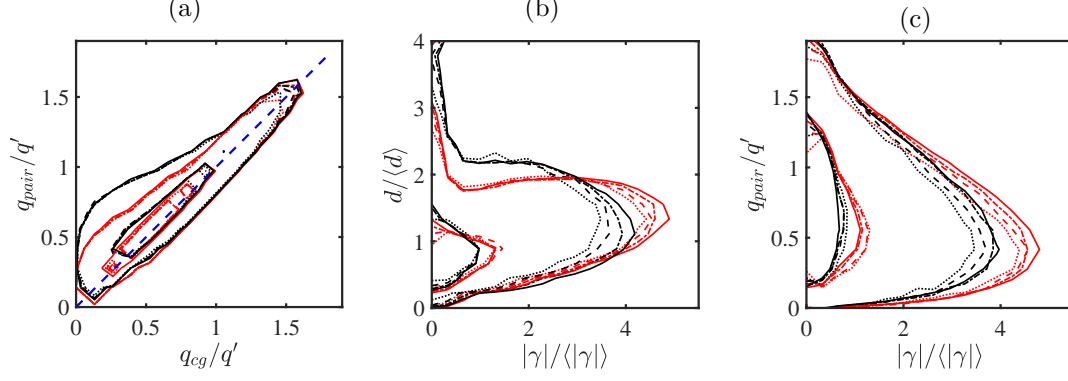


Figure 10: Properties of the vortex pairs. (a) Joint p.d.f. of the velocity of the centre of gravity of a vortex pair versus the averaged velocity magnitude of its two component vortices. In all the panels in this figure: ·····, T256; ---, T512; -·-·-, T768; —, T1024. Red lines are dipoles, and black ones are corrotating pairs. The two probability contours in each case enclose 50% and 95% of the probability mass. (b) Mean circulation magnitude of the vortex components of the pair, versus the inter-component distance. (c) Vortex circulation versus vortex mobility.

to the lower right in the figure represents a family of strong cores with large circulations, whose intra-pair distance is relatively small. This family exists for corrotating pairs and for dipoles, although it is most marked for the latter. The vertical band to the left of the figure contains relatively weak vortices with no clear preference for a particular coupling distance. Most vortex pairs are in this latter family, but they are relatively unimportant for the flow. Approximately 66% of the cores have $|\gamma| < \langle |\gamma| \rangle$, but they only contain 15-25% of the total circulation magnitude. A similar distinction can be based on vortex area (not shown), since the mean vorticity is relatively uniform across the vortices. The classification into vortex types can be based on either property.

One could hypothesise that the large, tightly-coupled vortices in the ‘nose’ family would be the ones with the fastest mobilities, which they would induce on each other, but figure 10(c) shows that the opposite is true. The vortices with the largest circulations move relatively slowly, and the high mobilities tend to be associated with the weak circulations to the left of the figure. This somewhat surprising observation leads to a model in which a set of organising large vortices in an ‘approximate equilibrium’ configuration are responsible for organising the flow into streams where weaker vortices are advected at relatively high speed.

In fact, the large and small vortices have very different properties. Figure 11(a,b) shows the one-dimensional p.d.f. of the core circulation, which collapses reasonably well for all the simulations and evolution times. Figure 11(a) shows that the weak vortices, $|\gamma| < \langle |\gamma| \rangle$, follow a power-law distribution $P(|\gamma|) \sim |\gamma|^{-3/4}$, while figure 11(b) shows that the vortices above that limit follow an exponential one. The separation of decaying two-dimensional turbulence into coherent vortices evolving under mutual induction, and a ‘chaotic’ background has been discussed often (Benzi *et al.*, 1987, 1988; McWilliams, 1990b), but the background is usually not characterised in term of vortices, and we are not aware of any previous characterisation of the larger vortices as slowly moving. For example, Benzi *et al.* (1987) discuss the large vortices as the only coherent structures in the flow and report that their areas follow a power-law distribution, although

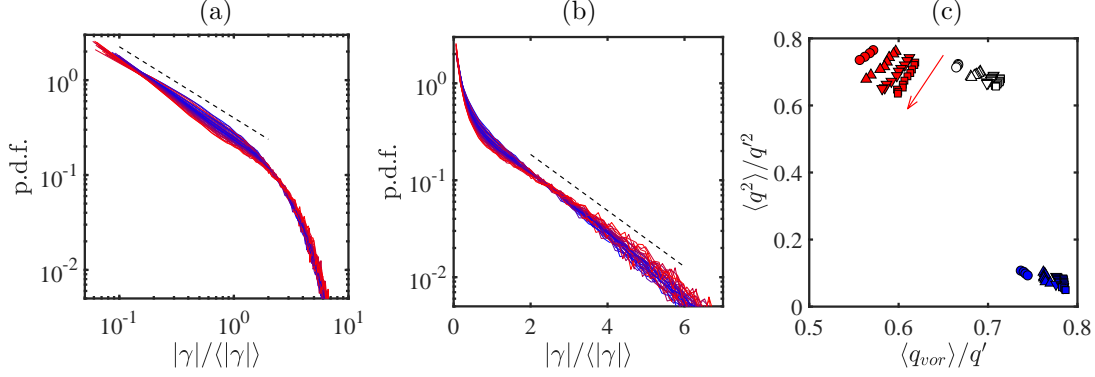


Figure 11: (a) P.d.f. of the vortex circulation magnitude. In all cases, time increases from blue to red. The dashed line is proportional to $|\gamma|^{-0.75}$. (b) As in (a). The dashed line is proportional to $\exp(-0.666|\gamma|/\langle|\gamma|\rangle)$. (c) Kinetic energy contained in different vortex classes versus mean vortex mobility. Open symbols are all the thresholded vortices; red symbols are large vortices, $s_{vor} \geq \langle s_{vor} \rangle$; blue symbols are $s_{vor} < \langle s_{vor} \rangle$. The red arrow is the direction of time advance for the red symbols.

with a different exponent than the one above, $|\gamma|^{-3/2}$. The reason for this difference is not clear, although we mentioned in §2 that Benzi *et al.* (1987) study a later stage of the decay, and that they use a higher-order viscous dissipation, which presumably creates different vortex cores (McWilliams, 1990b; Jiménez, 1994). It is also unclear why the exponential range of the distribution in figure 11(b) is not discussed by Benzi *et al.* (1987), although this may be partly due to their different sample size. The analysis in their paper is based on 17 vortices, while each of the distributions in figure 11 represents 10^4 – 10^5 objects.

Figure 11(c) shows that the kinematics of the weak and strong cores is very different. The vertical axis in this figure is the fraction of the kinetic energy carried by the thresholded vortices, defined as in figure 9(i). The open symbols are the contribution from all the vortices, as in that figure, and the red symbols are the contribution from vortices whose area is larger than the average. They contain most of the kinetic energy. The blue symbols in the lower-right corner are the contribution from vortices smaller than the average, which is much smaller. The horizontal axis is the average vortex mobility defined as the modulus of $\dot{\mathbf{q}}$. The large and small vortices lie in very different parts of the plot, as already suggested by figure 10(c). Large vortices are responsible for most of the kinetic energy of the flow, but are themselves relatively immobile, while small ones move fast, but are only responsible for a small fraction of the kinetic energy.

Power-law and exponential probability distributions suggest that the cores grow by aggregation of smaller units but, while a power law implies self-similar scale-free growth, in which cores merge with other cores of similar size (Benzi *et al.*, 1992), an exponential has a definite scale, which is proportional to the mean of the distribution, and to the size of the elements being accreted (Jiménez & Kawahara, 2013). In figure 11 the lower limit of the exponential is indeed of the order of $\langle|\gamma|\rangle$, and it is interesting to speculate about an aggregation model in which cores merge self-similarly with each other until they grow to be large enough to ‘freeze’ in a quasi-equilibrium slowly evolving pattern. The motion of these large vortices is not chaotic, at least over short times, and these cores stop merging among themselves. But they keep absorbing

the remaining fast-moving vortices of the background, and the largest of these field vortices determine the scale of the exponential distribution.

Vortex arrangements that remain stationary in some frame of reference have been studied for over a century (see the review in Aref *et al.*, 2002). Some of them are stable, and form spontaneously in experiments. In particular, forced two-dimensional turbulence is known to settle to stationary vortex ‘crystals’ which are partly determined by the forcing method and by the boundary conditions (Fine *et al.*, 1995; Jin & Dubin, 2000; Jiménez & Guegan, 2007), and beautiful examples of equilibrium vortex polygons have been observed in the polar regions of planetary atmospheres (Tabataba-Vakilia *et al.*, 2020). Most known equilibrium systems are regular arrangements of vortices of a single sign in a background of opposite-sign vorticity, but mixed-sign stable systems are also known. The von Kármán vortex street is probably the best-known example of the latter, and it is known that two-dimensional turbulence in a square box converges to a quasi-equilibrium single dipole, arranged diagonally in the box, which only decays slowly by viscosity (Smith & Yakhot, 1993).

The circulation of the slow-moving vortices discussed here is essentially in balance (with a residue of 1%-3% of ω'), but they are still far from equilibrium, and may perhaps be considered an intermediate stage to a final steady state. Attempts to extract a regular arrangement for them failed, beyond the four-way symmetry induced by the computational box, but the drop in mobility can be considered diagnostic of incipient ‘crystallisation’.

4.2 The up-scale energy flux

The discussion in the previous section raises the question of how the dipoles get organised into long streams. Three examples are given in figure 12. They are chosen to demonstrate the aggregation process, rather than randomly, but they are fairly representative. Approximately 30% of the simulations display similar patterns in their initial evolution. Each row in the figure is a simulation, displayed at four approximately equidistant times, which are the same for the three cases. Vortices are represented in colour, according to their sign, and the arrows are the velocities. The intensity of the grey background is the velocity magnitude. To best display the evolution, only the largest vortices ($s > \langle s \rangle$) are included in each plot, and the Reynolds number is purposely chosen low.

Each simulation starts with a relatively disorganised arrangement of vortices but, at the end of each sequence, positive (red) vortices have sorted themselves to one side of the flow, and negative (blue) ones to the other, supporting a jet between them. Some merging of like-signed vortices takes place in all cases.

The question is how this happens, because, while continuity probably implies that the velocity of any elongated velocity structure should be aligned with its axis, the opposite is not true. Compact jet-like vortex dipoles with aspect ratios of order one (modons) are well-known stable solutions of the Euler and Navier–Stokes equations (Flierl *et al.*, 1980; McWilliams, 1980).

Simulations of point vortex systems (not shown) spontaneously form tight dipoles and corrotating pairs, but the dipoles never organise into trains or jets, as is the case in figure 12(a,b). Neither do they form stronger dipoles of vortex ‘clouds’, as in figure 12(c). When a point dipole collides with a solitary point vortex or with a corrotating pair, it often loses one of its vortices, possibly breaking the colliding couple and forming a new association. Very seldom the resulting arrangement involves more than two vortices.

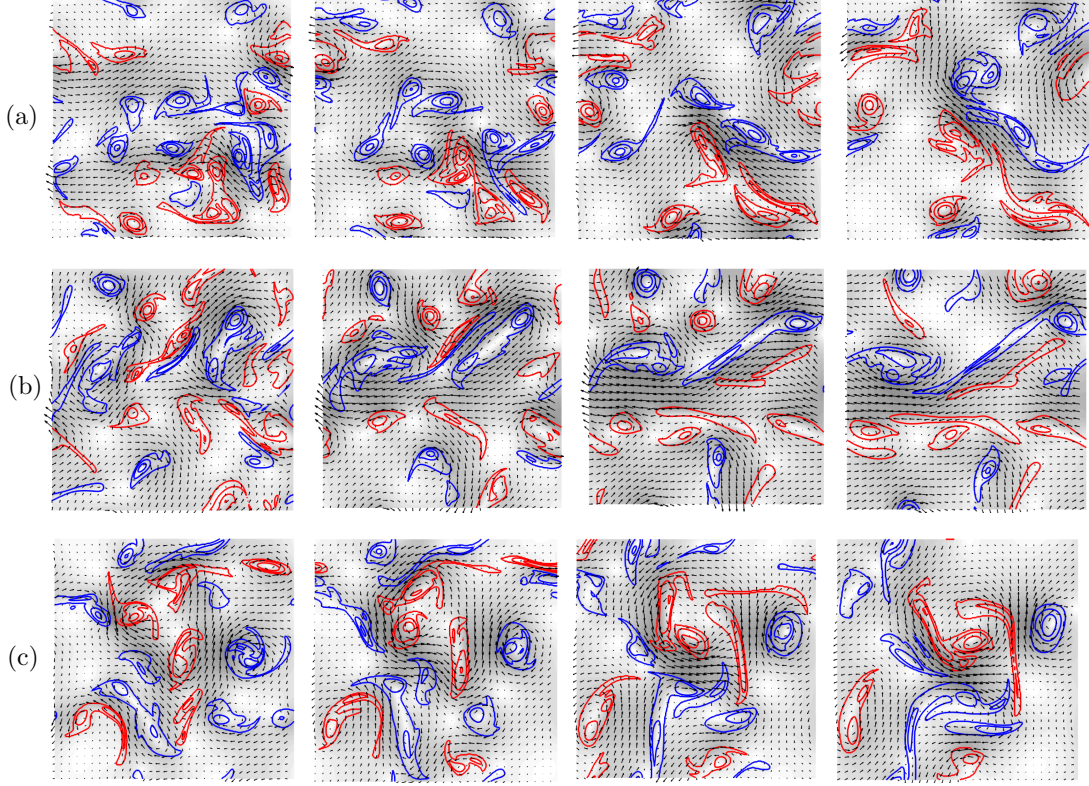


Figure 12: Three examples of the organisation of vortices into streams. Time runs in each row from left to right, $\omega_0 t = 0, 2, 4.6, 6.5$. Case T256. The three rows are independent realisations, and only vortices with $s > \langle s \rangle$ are included in the figure. Line contours are positive (red) and negative (blue) vorticity, the arrows are velocity, and the grey background is the velocity magnitude.

Of course, sets of point vortices are Hamiltonian systems whose interactions conserve energy (Batchelor, 1967). Both the merging of like-signed vortices and the breaking of an existing dipole involve energy exchanges, which are much simpler if viscosity or filamentation can be used as an energy dump, but any such selection criterion requires a local mechanism to implement it. In particular, it is unclear why a positive vortex overtaken by a dipole would tend to reinforce the positive component of the dipole, strengthening it, rather than merging with the negative one, weakening it.

A possible mechanism is explained in figure 13. Consider the point-vortex dipole in figure 13(a). In the comoving frame of reference, it forms a recirculation bubble separated from infinity by an approximately elliptical dividing streamline (see appendix B). Any sufficiently weak point vortex being overtaken by the dipole follows the streamlines around the bubble, independently of its sign, and it is eventually left behind. There is no preference for which side of the dipole its path takes, and it is therefore unlikely to statistically strengthen or weaken it.

The situation is different for the entrainment of an extended vortex, as detailed in appendix B for the case of a uniform vortex patch. Such patches drift with respect to the advecting

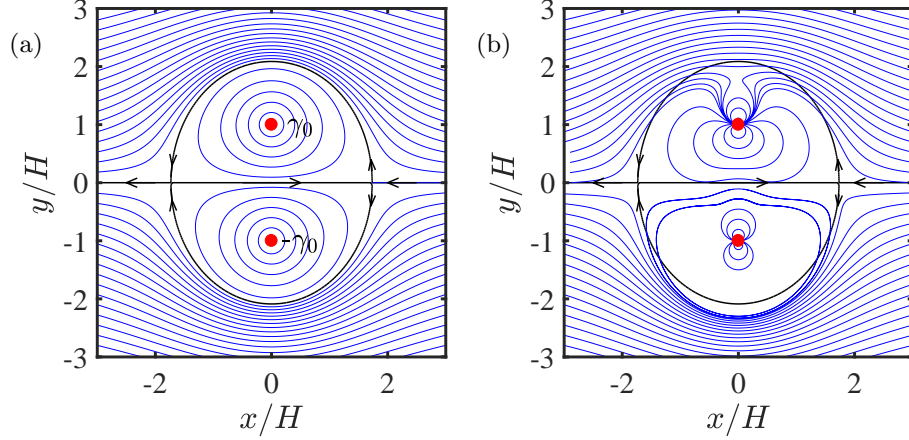


Figure 13: (a) Velocity field of a dipole of equal point vortices of circulation $\pm\gamma_0$ at distance $2H$. The dipole is moving to the right, but is shown in the frame of reference linked to the vortices. The blue lines are streamlines, as well as the trajectories of an advected point vortex. The black lines are the dividing streamline in this frame of reference. (b) As in (a), but the blue lines are the trajectories of the centre of gravity of a vortex patch of positive circulation γ and area s , such that $\gamma_0 s^2 / \gamma H^4 = 2$. A patch with negative circulation would be entrained to the negative vortex in the dipole. See text and appendix B for details.

streamlines, as shown by the trajectories in figure 13(b). Positive patches drift towards the positive component of the dipole, and negative ones towards the negative component. The result is an average strengthening of the dipole, and the formation of organised jets.

Note that this accretion model could explain the asymmetry observed in figure 8, where it was shown that the direction of the velocity of a stream is a better predictor of the direction taken by the stream ahead than behind the point at which it is measured. In the model presented here dipoles propagate forward, and take some time to form while the entrained vortices are incorporated into it. The jet of a growing dipole is strongest at its trailing edge, and therefore predicts better the position of the leading dipole ahead of it.

5 Discussion and conclusions

We have used simulation ensembles of decaying two-dimensional turbulence to study the early stages of the evolution of the flow from a disorganised state towards a set of vortex cores and large-scale kinetic energy structures. In this period, the dominant scale of the kinetic energy is still small compared to the size of the computational box, and grows monotonically. We have shown that, at least at the moderate Reynolds numbers of our simulations, this growth is due to the appearance of elongated ‘streams’ formed by the concatenation of vortex dipoles. The growth of the energy scale is not due to the elongation of the streams, whose aspect ratio stays in the range of 8–10, but to their proliferation, and to the increase of the area fraction that they cover.

We have traced the formation of the streams to a process of aggregation of the vortex cores. The cores evolve into two separate classes. Most of them are small and mobile, and merge

among themselves in a self-similar cascade that results in a power-law probability distribution of vortex sizes (Benzi *et al.*, 1992). A few of the cores grow larger, and eventually ‘freeze’ into a low-mobility vortex system. These larger vortices are responsible for most of the kinetic energy of the flow, but they themselves move slowly, in what can be described as a quasi-equilibrium vortex ‘crystal’. The probability distribution of their areas and circulations is exponential, rather than potential, suggesting that they do not grow by interacting among themselves, but by absorbing smaller vortices from the self-similar background. They are responsible for the formation of the streams. We have proposed a formation mechanism by noting that, although a vortex dipole shows no preference about how to entrain a point vortex of either sign, the drift velocity of vortex patches biases positive extended vortices to merge with the positive component of the dipole, and negative vortices to merge with the negative component. As a consequence, the dipoles are strengthened and the streams are formed.

This growth mechanism of the energy scale is probably not the classical inverse energy cascade, which is typically studied in forced, rather than in decaying flows. There are two main properties to be explained for this cascade (Tabeling, 2002; Boffetta & Ecke, 2012). The first one is its $k^{-5/3}$ power spectrum, and the second is its low intermittency. The latter is consistent with the process discussed here, since growth by aggregation of small units of fixed size is not an intermittent process, but both the exponential probability distribution of the vortex size and the approximately crystallisation argue against the self-similarity implied by a power-law spectrum. Note that there is no $k^{-5/3}$ plateau in the spectral slopes in figure 1(c). It is possible that in much larger simulations, the aggregation of dipoles into streams is hierarchical and self-similar, but it is difficult to see how self-similarity can avoid intermittency. Moreover, the speed at which the streams arise, for example in figure 12, suggests that it would be hard to prevent the large-scale vortex organisation from falling into local equilibrium. A more appealing possibility is that the role of forcing in promoting a self-similar inverse cascade is related to the ‘melting’ of the vortex crystal. Although beyond the scope of present paper, a model of repeated local crystallisation and melting through ‘thermal’ excitations is probably not particularly intermittent.

It is difficult not to be reminded by the discussion above of other examples of spontaneous stream formation in more complicated flows. The best-known are probably the streaks in wall-bounded turbulence and other shear flows (Tsukahara *et al.*, 2006; Dong *et al.*, 2017; Jiménez, 2018), and the azimuthal jets of planetary atmospheres and rotating flows (Grossmann *et al.*, 2016; Sacco *et al.*, 2019). In many of these cases, the streams are a streamwise concatenation of smaller units (Lozano-Durán *et al.*, 2012), and the question arises of how these units organise longitudinally. This is not the place to review the many models proposed for this organisation, but most of them depend on the generation of new vorticity, which is readily available for a shear and is required for a sustained flow. There is no vorticity generation in two-dimensional flow, and the mechanism discussed here, which depends on the reorganisation of vorticity rather than on its creation, suggests that some of these streams may, at least in part, share a common mechanism which is more related to symmetry-breaking arguments of pattern formation than to the dynamics of the energy-generation process.

It is finally interesting to remark that, although the analysis in this paper is a fairly classical example of hypotheses-driven research, it was made possible by following the ‘blind suggestion’ from the Monte–Carlo experiments in Jiménez (2020*b*), that dipoles are at least as relevant to two-dimensional turbulence as individual cores

This work was supported by the European Research Council under the Coturb grant ERC-

References

- AREF, H., NEWTON, P. K., STREMLER, M. A., TOKIEDA, T. & VAINCHTEIN, D. L. 2002 Vortex crystals. *Advances in Appl. Mech.* **39**, 1–79.
- BASDEVANT, C. & SADOURNY, R. 1975 Ergodic properties of inviscid truncated models of two-dimensional incompressible flows. *J. Fluid Mech.* **69**, 673–688.
- BATCHELOR, G. K. 1967 *An introduction to fluid dynamics*. Cambridge U. Press.
- BATCHELOR, G. K. 1969 Computation of the energy spectrum in homogeneous two dimensional turbulence. *Phys. Fluids Suppl.* **II**, **12**, 233–239.
- BENZI, R., COLELLA, M., BRISCOLINI, M. & SANTANGELO, P. 1992 A simple point vortex model for twodimensional decaying turbulence. *Phys. Fluids A* **4**, 1036–1039.
- BENZI, R., PATARNELLO, S. & SANTANGELO, P. 1987 On the statistical properties of decaying two-dimensional turbulence. *Europhys. Lett.* **3**, 811–818.
- BENZI, R., PATARNELLO, S. & SANTANGELO, P. 1988 Self-similar coherent structures in two-dimensional decaying turbulence. *J. Phys. A: Math. and General* **21**, 1221–1237.
- BETCHOV, R. 1956 An inequality concerning the production of vorticity in isotropic turbulence. *J. Fluid Mech.* **1**, 497–504.
- BOFFETTA, G., CELANI, A. & VERGASSOLA, M. 2000 Inverse energy cascade in two-dimensional turbulence: Deviations from Gaussian behavior. *Phys. Rev. E* **61**, R29.
- BOFFETTA, G. & ECKE, R. E. 2012 Two-dimensional turbulence. *Ann. Rev. Fluid Mech.* **44**, 427–451.
- BRACHET, M. E., MENEGUZZI, M., POLITANO, H. & SULEM, P. L. 1988 The dynamics of freely decaying two-dimensional turbulence. *J. Fluid Mech.* **194**, 333–349.
- CARDESA, J. I., VELA-MARTÍN, A. & JIMÉNEZ, J. 2017 The turbulent cascade in five dimensions. *Science* **357**, 782–784.
- CARNEVALE, G. F., MCWILLIAMS, J. C., POMEAU, Y., WEISS, J. B. & YOUNG, W. R. 1991 Evolution of vortex statistics in two-dimensional turbulence. *Phys. Rev. Lett.* **66**, 2735–2737.
- CATRAKIS, H. J. & DIMOTAKIS, P. E. 1996 Scale distributions and fractal dimensions in turbulence. *Phys. Rev. Lett.* **77**, 3795–3798.
- DONG, S., LOZANO-DURÁN, A., SEKIMOTO, A. & JIMÉNEZ, J. 2017 Coherent structures in statistically stationary homogeneous shear turbulence. *J. Fluid Mech.* **816**, 167–208.
- EYINK, G. L. 2006 Multiscale gradient expansion of the turbulent stress tensor. *J. Fluid Mech.* **549**, 159–190.
- FINE, K. S., CASS, A. C., FLYNN, W. G. & DRISCOLL, C. F. 1995 Relaxation of 2d turbulence to vortex crystals. *Phys. Rev. Lett.* **75**, 3277–3280.

- FLIERL, G. R., LARICHEV, V. D., MCWILLIAMS, J. C. & REZNIK, G. M. 1980 The dynamics of baroclinic and barotropic solitary eddies. *Dyn. Atmos. Oceans* **5**, 1–41.
- GROSSMANN, S., LOHSE, D. & SUN, C. 2016 High-Reynolds number Taylor–Couette turbulence. *Ann. Rev. Fluid Mech.* **48**, 53–80.
- JIMÉNEZ, J. 1988 Linear stability of a non-symmetric, inviscid, Kármán street of small uniform vortices. *J. Fluid Mech.* **189**, 337–348.
- JIMÉNEZ, J. 1994 Hyperviscous vortices. *J. Fluid Mech.* **279**, 169–176.
- JIMÉNEZ, J. 2018 Coherent structures in wall-bounded turbulence. *J. Fluid Mech.* **842**, P1.
- JIMÉNEZ, J. 2018 Machine-aided turbulence theory. *J. Fluid Mech.* **854**, R1.
- JIMÉNEZ, J. 2020a Computers and turbulence. *Europ. J. Mech. B: Fluids* **79**, 1–11.
- JIMÉNEZ, J. 2020b Monte Carlo science. *J. Turbul.* doi:10.1080/14685248.2020.1742918.
- JIMÉNEZ, J. & GUEGAN, A. 2007 Spontaneous generation of vortex crystals from forced two-dimensional homogeneous turbulence. *Phys. Fluids* **19**, 085103.
- JIMÉNEZ, J. & KAWAHARA, G. 2013 Dynamics of wall-bounded turbulence. In *Ten chapters in turbulence* (ed. P. A. Davidson, Y. Kaneda & K. R. Sreenivasan), pp. 221–268. Cambridge U. Press.
- JIMÉNEZ, J., WRAY, A. A., SAFFMAN, P. G. & ROGALLO, R. S. 1993 The structure of intense vorticity in isotropic turbulence. *J. Fluid Mech.* **255**, 65–90.
- JIN, D. Z. & DUBIN, D. H. E. 2000 Characteristics of two-dimensional turbulence that self-organizes into vortex crystals. *Phys. Rev. Lett.* **84**, 1443–1446.
- JOYCE, G. & MONTGOMERY, D. 1973 Negative temperature states for the two-dimensional guiding-centre plasma. *J. Plasma Phys.* **10**, 107–121.
- KRAICHNAN, R. H. 1967 Inertial ranges in two-dimensional turbulence. *Phys. Fluids* **10**, 1417–1423.
- LESIEUR, M. 2008 *Turbulence in fluids*, 4th edn. Springer.
- LOZANO-DURÁN, A., FLORES, O. & JIMÉNEZ, J. 2012 The three-dimensional structure of momentum transfer in turbulent channels. *J. Fluid Mech.* **694**, 100–130.
- MCWILLIAMS, J. C. 1980 An application of equivalent modons to atmospheric blocking. *Dyn. Atmos. Oceans* **5**, 43 – 66.
- MCWILLIAMS, J. C. 1984 The emergence of isolated coherent vortices in turbulent flow. *J. Fluid Mech.* **146**, 21–43.
- MCWILLIAMS, J. C. 1990a A demonstration of the suppression of turbulent cascades by coherent vortices in two-dimensional turbulence. *Phys. Fluids A* **2**, 547–552.
- MCWILLIAMS, J. C. 1990b The vortices of two-dimensional turbulence. *J. Fluid Mech.* **219**, 361–385.
- MEUNIER, P., LE DIZÈS, S. & LEWEKE, T. 2005 Physics of vortex merging. *C. R. Physique* **6**, 431–450.

- MOISY, F. & JIMÉNEZ, J. 2004 Geometry and clustering of intense structures in isotropic turbulence. *J. Fluid Mech.* **513**, 111–133.
- MONTGOMERY, D. & JOYCE, G. 1974 Statistical mechanics of “negative temperature” states. *Phys. Fluids* **17**, 1139–1145.
- MONTGOMERY, D., MATTHAEUS, W. H., STRIBLING, W. T., MARTINEZ, D. & OUGHTON, S. 1992 Relaxation in two dimensions and the sinh-Poisson equation. *Phys. Fluids A* **4**, 3–6.
- MONTGOMERY, D., SHAN, X. & MATTHAEUS, W. H. 1993 Navier–Stokes relaxation to sinh-Poisson states at finite Reynolds numbers. *Phys. Fluids A* **5**, 2207–2216.
- ONSAGER, L. 1949 Statistical hydrodynamics. *Nuovo Cimento Suppl.* **6**, 279–286.
- PARET, J. & TABELING, P. 1998 Intermittency in the two-dimensional inverse cascade of energy: Experimental observations. *Phys. Fluids* **10**, 3126–3136.
- RICHARDSON, L. F. 1920 The supply of energy from and to atmospheric eddies. *Proc. Roy. Soc. A* **97**, 354–373.
- SACCO, F., VERZICCO, R. & OSTILLA-MÓNICO, R. 2019 Dynamics and evolution of turbulent Taylor rolls. *J. Fluid Mech.* **870**, 970–987.
- SAFFMAN, P. G. 1971 On the spectrum and decay of random two-dimensional vorticity distributions at large Reynolds number. *Studies Appl. Math.* **50**, 377–383.
- SMITH, L. M. & YAKHOT, V. 1993 Bose condensation and small-scale structure generation in a random-force driven 2d turbulence. *Phys. Rev. Lett.* **71**, 352–355.
- SMITH, L. M. & YAKHOT, V. 1994 Finite-size effects in forced two-dimensional turbulence. *J. Fluid Mech.* **274**, 115–138.
- TABATABA-VAKILIA, F., ROGERS, J. H., EICHSTÄDT, G., ORTON, G. S., HANSEN, C. J., MOMARY, T. W., SINCLAIR, J. A., GILES, R. S., CAPLINGER, M. A., RAVINE, M. A. & BOLTON, S. J. 2020 Long-term tracking of circumpolar cyclones on Jupiter from polar observations with JunoCam. *Icarus* **335**, 113405.
- TABELING, P. 2002 Two-dimensional turbulence: a physicist approach. *Physics Rep.* **362**, 1–62.
- TSUKAHARA, T., KAWAMURA, H. & SHINGAI, K. 2006 DNS of turbulent Couette flow with emphasis on the large-scale structure in the core region. *J. Turbul.* **7**, 19.
- VINCENT, A. & MENEGUZZI, M. 1991 The spatial structure and statistical properties of homogeneous turbulence. *J. Fluid Mech.* **225**, 1–20.
- XIAO, Z., WAN, M., CHEN, S. & EYINK, G. L. 2009 Physical mechanism of the inverse energy cascade of two-dimensional turbulence: a numerical investigation. *J. Fluid Mech.* **619**, 1–44.

A Poisson distribution of the closest point

If the expected number of Poisson-distributed points in a set parametrised with r is $\lambda(r)$, the probability of finding no points within the set is

$$P_0(r) = \exp(-\lambda), \quad (5)$$

and the probability density that the first point is precisely at r is

$$P_c(r) = -(dP_0/dr) = (d\lambda/dr) \exp(-\lambda). \quad (6)$$

For a set of points distributed in a plane with uniform average density ρ , the expected number of points within a distance r of a reference position is $\lambda = \pi\rho r^2$, and

$$P_c(r) = 2\pi\rho r \exp(-\pi\rho r^2). \quad (7)$$

This distribution can easily be integrated to show that the average distance to the closest point is $\langle r \rangle_0 = 1/\sqrt{4\rho}$, so that eq:poiss2 can be written as

$$P_c(\xi) = (\pi\xi/2) \exp(-\pi\xi^2/4), \quad (8)$$

where $\xi = r/\langle r \rangle_0$.

If we add the restriction that no point can be closer than a distance a (e.g. the vortex diameter), the expected number of points within a distance $r \geq a$ is $\lambda = \pi\rho(r^2 - a^2)$, and

$$P_c(r) = 2\pi\rho r \exp[-\pi\rho(r^2 - a^2)], \quad (9)$$

and the average distance to the closest point becomes

$$\langle r \rangle_\epsilon = \int_a^\infty r P_c(r) dr = a + (1/2\sqrt{\rho}) \operatorname{erfc}(\epsilon) \exp(\epsilon^2), \quad (10)$$

where $\epsilon = a/\sqrt{\rho\pi} = \sqrt{4/\pi} a/\langle r \rangle_0$. It can be shown that $\langle r \rangle_\epsilon \approx a$ for $\epsilon \gg 1$, but that $\langle r \rangle_\epsilon \approx \langle r \rangle_0$ for $\epsilon \lesssim 0.5$. Figure 9(e) suggests that $\hat{a} = a/\langle r \rangle_0 \approx 0.2\text{--}0.3$, so that

$$P_c(\xi) \approx (\pi\xi/2) \exp[-\pi(\xi^2 - \hat{a}^2)/4], \quad \xi > \hat{a}. \quad (11)$$

The effect is to crop part of the distribution near the origin, while raising its peak to compensate for the missing mass (as in figure 1.e).

B Drift of a vortex patch.

While point vortices are advected by the flow velocity, vortices with a wider support drift with respect to it. In the particular case of small patches of uniform vorticity, the drift velocity can be computed as a series expansion of the vortex radius. The following results are cited from Jiménez (1988).

Define a complex variable $z = (x + iy)/H$, where H is a characteristic length scale, and consider a uniform vortex patch of circulation $\gamma\Gamma$ and area s . Using Γ and H to define the time and length scales, the expansion parameter is $\epsilon^2 = s/\pi H^2$, which is assumed to be small. The

irrotational complex flow velocity in the absence of the patch is described by an analytic function $w_\infty(z) = (u - iv) H/\Gamma$, with a similar non-analytic expression within the patch. To lowest order, the contour of the patch is an ellipse,

$$z - z_c = \epsilon \eta (1 + b_2 \epsilon^2 / \eta^2), \quad (12)$$

where z_c is the centre of gravity of the patch, and $\eta = \exp(i\phi)$ is the unit circle. Matching at this contour the expansions of the velocity inside and outside the patch provides an evolution equation for the ellipticity,

$$2\pi\epsilon^2 db_2/d\tau = i\gamma b_2 + c_2^*, \quad (13)$$

where $\tau = \Gamma t/H^2$ is a rescaled time, the asterisk stand for complex conjugation, and

$$c_k = \frac{2\pi}{(k-1)!} \frac{d^{k-1}w_\infty}{dz^{k-1}}(z_c). \quad (14)$$

The drift velocity, defined as $dz_c^*/d\tau = w_\infty(z_c) + w_d$, can be expressed as

$$w_d = (\epsilon^4/2\pi)b_2c_3, \quad (15)$$

and, if we further assume that eq:patch2 has reached equilibrium, so that $b_2 = ic_2^*/\gamma$,

$$w_d = \frac{\pi i \epsilon^4}{\gamma} \frac{dw_\infty^*}{dz^*} \frac{d^2w_\infty}{dz^2}. \quad (16)$$

Consider now the effect on the patch from a dipole formed by two point vortices of circulation $\Gamma\gamma_0$ separated by a distance $2H$. In figure 13(a) in the body of the paper, the positive vortex is on top, and the dipole would move to the right, but it is made stationary by a uniform negative velocity at infinity. Consider a third vortex being overtaken by the dipole, but neglect its effect on the dipole itself. In the units defined above, the velocity induced by the dipole is

$$w_\infty = \frac{\gamma_0}{\pi} \left(\frac{1}{1+z^2} - \frac{1}{4} \right). \quad (17)$$

Its effect on a point vortex is given by the streamlines in figure 13(a). The vortex is deflected around the recirculation bubble of the dipole, and eventually left behind. There is no difference between a positive and a negative vortex. The situation is different for an extended patch, because the drift velocity,

$$w_d = -\frac{4i\gamma_0^2\epsilon^4}{\gamma\pi} \frac{z^*}{1+z^{*2}} \frac{3z^2-1}{(1+z^2)^3}, \quad (18)$$

depends on the sign of the circulation of the patch being overtaken. As shown in figure 13(b), positive vortices tend to be entrained into the upper part of the stream, and to merge with the positive vortex of the dipole. Negative patches are entrained towards the lower negative vortex. The result is that the dipole is reinforced on average.